



# Identification of embedded nanotwins at c-Si/a-Si:H interface limiting the performance of high-efficiency silicon heterojunction solar cells

Xianlin Qu<sup>1,8</sup>, Yongcai He<sup>1,8</sup>, Minghao Qu<sup>2,8</sup>, Tianyu Ruan<sup>1</sup>, Feihong Chu<sup>1</sup>, Zilong Zheng<sup>1</sup>, Yabin Ma<sup>3</sup>, Yuanping Chen<sup>3</sup>, Xiaoning Ru<sup>2</sup>, Xixiang Xu<sup>2</sup>, Hui Yan<sup>1</sup>, Lihua Wang<sup>1</sup>, Yongzhe Zhang<sup>1</sup>,  
Xiaojing Hao<sup>1</sup>, Ziv Hameiri<sup>1</sup>, Zhi-Gang Chen<sup>1</sup>, Lianzhou Wang<sup>1</sup>, Kun Zheng<sup>1</sup>

The interface of high-quality crystalline silicon/hydrogenated amorphous silicon (c-Si/a-Si:H) is indispensable for achieving the ideal conversion efficiency of Si heterojunction solar cells. Therefore, it is extremely desirable to characterize and control the interface at the atomic scale. Here, we employ spherical aberration-corrected transmission electron microscopy to investigate the atomic structure of the c-Si/a-Si:H interface in high-efficiency Si heterojunction solar cells. Their structural evolution during *in situ* annealing is visualized at the atomic scale. High-density embedded nanotwins, detrimental to the device performance, are identified in the thin epitaxial layer between c-Si and a-Si:H. The nucleation and formation of these nanotwins are revealed via ex situ and *in situ* high-resolution transmission electron microscopy. Si heterojunction solar cells with low-density nanotwins are fabricated by introducing an ultra-thin intrinsic a-Si:H buffer layer and show better performance, indicating that the strategy to restrain embedded nanotwins can further enhance the conversion efficiency of Si heterojunction solar cells.

**C**rystalline silicon (c-Si) solar cells are the state-of-the-art photovoltaic technology to date due to their significant advantages, including nearly optimum bandgap, high efficiency, proven stability and widely available raw materials<sup>1–3</sup>. For a Si solar cell with a 165-μm-thick Si wafer (resistivity, 3 Ω cm), the highest power conversion efficiency (PCE) was theoretically predicted to be 29.1% (ref. <sup>4,5</sup>). Si heterojunction (SHJ) technology, first suggested in 1974 (ref. <sup>6</sup>), is one of the most promising technologies to achieve a high PCE. With continuous manufacturing improvements<sup>7</sup>, 24.5% PCE (total area, 239 cm<sup>2</sup>) and 25.1% PCE (aperture area, 151.9 cm<sup>2</sup>) SHJ solar cells have been achieved by Kaneka<sup>8</sup>. By combining SHJ technology with interdigitated-back-contact design, a record 26.7% PCE with a designated illumination area of 79 cm<sup>2</sup> was reported by Kaneka in 2017 (refs. <sup>9,10</sup>). Recently, SHJ technology has been exploited to fabricate Si-based tandem multi-junction devices such as III–V/Si and perovskite–Si, which have obtained higher PCEs<sup>11,12</sup>. However, further efficiency enhancements of single-junction SHJ solar cells seem to have stalled in the last three years. Therefore, it is urgent that we discover new breakthroughs to solve the bottlenecks and obtain higher SHJ solar cell PCEs.

Interface recombination at the c-Si/a-Si:H interface has been considered one of the key elements for the loss of PCE in SHJ solar cells<sup>13</sup>. Moreover, Si dangling bonds on the surface of Si wafers have been shown to be the dominant defects governing c-Si/a-Si:H interface recombination<sup>14,15</sup>. In order to reduce c-Si/a-Si:H interface recombination, a thin intrinsic a-Si:H (i-a-Si:H) layer is usually deposited on the c-Si surface to passivate Si dangling bonds, increasing both the open circuit voltage ( $V_{oc}$ )<sup>16</sup> and fill factor (FF)<sup>17</sup>.

However, undesirable epitaxial growth of the Si film usually occurs on the c-Si surface<sup>18</sup>. Consequently, rough c-Si/a-Si:H interfaces resulting from epitaxial growth reduce the effect of passivation<sup>19</sup>. In recent years, considerable endeavours have been performed to restrain this epitaxial growth<sup>20,21</sup>. However, the epitaxial growth of several atomic layers is hard to avoid.

Transmission electron microscopy (TEM) is a powerful technique for providing atomic scale structure characterization and *in situ* observation of structural evolution under service conditions<sup>22–24</sup>. Specifically, in SHJ solar cells, the thickness and abruptness of the epitaxial layer on the surface of c-Si have been determined well by using conventional high-resolution TEM (HRTEM)<sup>18,20,21</sup>. However, due to the insufficient resolution, it is still challenging to reveal the atomic structure at interfaces or defects, such as dislocations, twins, stacking faults and more, in epitaxial layers. With the advent of spherical aberration ( $C_s$ )-corrected TEM<sup>25</sup> and the developments of *in situ* techniques<sup>26–29</sup>, many atomic-level structure mechanisms behind complicated physicochemical and mechanical processes have been uncovered<sup>30,31</sup>.

In this study, high-density embedded nanotwins are identified at the c-Si/a-Si:H interface in high-efficiency SHJ solar cells using  $C_s$ -corrected TEM. The origins of the defects are further revealed using ex situ and *in situ*  $C_s$ -corrected HRTEM. Furthermore, SHJ solar cells with low-density embedded nanotwins are fabricated by optimizing the deposition process of i-a-Si:H, achieving a notably higher PCE. Our study indicates that the strategy to suppress nanotwin defects at the c-Si/a-Si:H interface can be used to guide future developments of SHJ solar cells.

<sup>1</sup>Beijing Key Lab of Microstructure and Properties of Solids, Faculty of Materials and Manufacturing, Beijing University of Technology, Beijing, China.

<sup>2</sup>Hanergy Chengdu Research and Development Center, Chengdu, China. <sup>3</sup>School of Science, Jiangsu University, Zhenjiang, China. <sup>4</sup>School of Photovoltaic and Renewable Energy Engineering, University of New South Wales, Sydney, New South Wales, Australia. <sup>5</sup>Centre for Future Materials, University of Southern Queensland, Springfield, Queensland, Australia. <sup>6</sup>School of Mechanical and Mining Engineering, University of Queensland, St Lucia, Queensland, Australia. <sup>7</sup>School of Chemical Engineering and Australian Institute for Bioengineering and Nanotechnology, University of Queensland, St Lucia, Queensland, Australia. <sup>8</sup>These authors contributed equally: Xianlin Qu, Yongcai He, Minghao Qu. ✉e-mail: [yzzhang@bjut.edu.cn](mailto:yzzhang@bjut.edu.cn); [kunzheng@bjut.edu.cn](mailto:kunzheng@bjut.edu.cn)

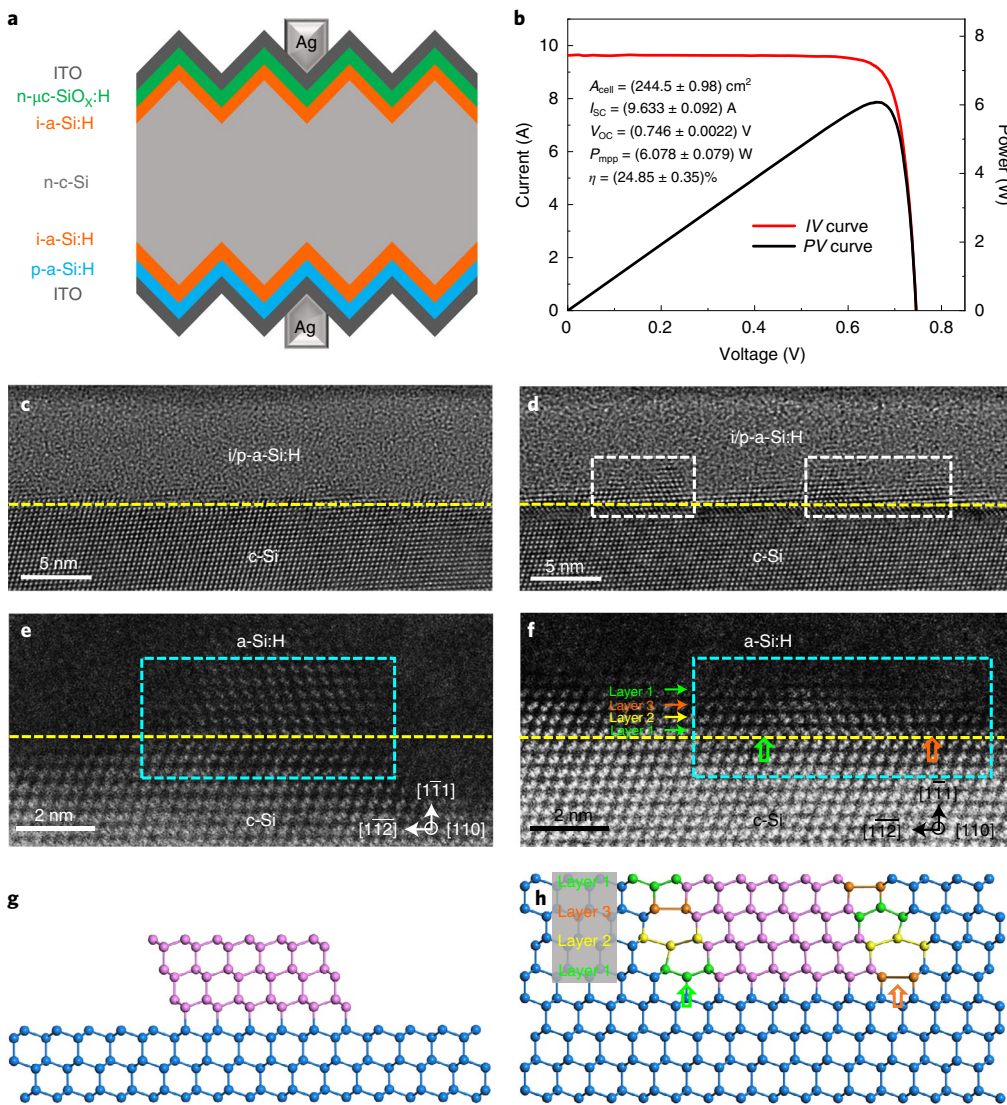


**Fig. 1 | c-Si/a-Si:H interface structure characteristics of SHJ solar cell.** **a**, Cross-section schematic image of the SHJ solar cell. n- $\mu$ c-SiO<sub>x</sub>:H, n-type microcrystal SiO<sub>x</sub>:H; i-a-Si:H, intrinsic a-Si:H; p-a-Si:H, p-type a-Si:H; n-c-Si, n-type crystal Si; ITO, indium tin oxide. **b**, IV curve and PV curve of the SHJ cell with conversion efficiency of 24.85%, which is the certified result provided by the Institute for Solar Energy Research in Hamelin.  $A_{\text{cell}}$ , area of the cell;  $I_{\text{SC}}$ , short circuit current;  $V_{\text{OC}}$ , open circuit voltage;  $P_{\text{mpp}}$ , maximum peak power;  $\eta$ , power conversion efficiency. **c,d**, HRTEM images of c-Si/a-Si:H interface viewed from the <110> orientation showing the slight normal epitaxial layer and epitaxial structures with defects, respectively. The dashed yellow lines indicate the initial c-Si wafer surface and the dashed white rectangles mark the location of defects. **e,f**, Atomic-resolution HAADF-STEM images of two types of defects, which are the free nanotwin and embedded nanotwin, respectively. The dashed yellow lines indicate the twin plane. The green and the orange hollow arrows in **f** mark the location of GBs between the main structure and embedded nanotwin. The labelled Layers 1 to 3 are three different atomic layers that make up the GBs. **g,h**, Geometrical atomic structure models derived from the aqua dashed rectangle areas in **e** and **f**, respectively. The blue and pink balls represent the c-Si wafer and nanotwin, respectively. The green, orange and yellow balls represent atoms at the three different atomic layers.

### Identification of nanotwin at c-Si/a-Si:H interface

We fabricated SHJ solar cells with the both-side-contact structure using an industry-compatible process. Figure 1a is a schematic diagram showing the cross-sectional structures of the SHJ solar cells used. Figure 1b plots the current–voltage (IV) curve and power–voltage (PV) characteristics of the SHJ solar cells. A PCE of 24.85% is certified by the Institute for Solar Energy Research in Hamelin with a total area of 244.5 cm<sup>2</sup> measured under standard test conditions. Cross-sectional samples were prepared by a focused ion beam (FIB) technique to study the c-Si/a-Si:H interface. To further understand the structural characteristics of the c-Si/a-Si:H interface, C<sub>s</sub>-corrected HRTEM was performed. Figure 1c,d shows typical HRTEM images that show two kinds of morphologies.

Considering the contrast difference and structural characteristics at the interface, the initial c-Si wafer surface is inferred and indicated by dashed yellow lines in the HRTEM images. Similar to previous reports<sup>18,20</sup>, the fluctuation with a thickness of 1–2 nm resulting from epitaxial growth can be observed (Fig. 1c). This epitaxial phenomenon on {111} planes is common and challenging to completely avoid during the passivation process<sup>18</sup>. But, in addition to this slight, normal epitaxial growth, defects such as twins or stacking faults are found in the epitaxial layer (Fig. 1d). To verify that these defects are generally present at the c-Si/a-Si:H interface, we prepared four additional cross-sectional samples randomly taken from an identical device; a similar interface structure was observed (Supplementary Fig. 1). Similar defective structures

have been captured via HRTEM in previous studies<sup>21,32</sup>, but none of them have been investigated in detail.

The best atomic contrast for accurately interpreting HRTEM images can be obtained only under the weak phase object approximation and Scherzer defocus conditions. Moreover, at hetero-interfaces, Fresnel fringes introduced by such conditions impose additional strong contrast, which impedes a more detailed structural analysis of the c-Si/a-Si:H interface<sup>33</sup>. By contrast, high-angle annular dark field scanning transmission electron microscopy (HAADF-STEM) images can address those problems. Based on the analysis of over 50 atomic-resolution HAADF-STEM images, two types of defect morphologies can be clearly illustrated. A HAADF-STEM image along the <110> direction is shown in Fig. 1e, from which a nanotwin covered by amorphous Si atoms (cannot be observed due to the dark contrast) can be found on the c-Si wafer surface, where the dashed yellow line presents the twin interface. Since the arrangement of boundary atoms is identical to the internal atoms in this type of nanotwin, we name it a ‘free nanotwin’. However, for the type of nanotwin shown in Fig. 1f, which is surrounded by ambient c-Si atoms, we use the name ‘embedded nanotwin’. For the embedded nanotwin, the arrangement of boundary atoms is different from the internal atoms. As indicated by green and orange hollow arrows in Fig. 1f, grain boundaries (GBs) between the main structure and embedded nanotwin are formed. Further statistical analyses suggest that the density of embedded nanotwins distributed along the <112> direction at the c-Si/a-Si:H interface is 20–30 per micrometre (Supplementary Fig. 2). Considering an average length of an embedded nanotwin is 5 nm, their total length accounts for 10–15% of the entire interface length. Based on these atomic-resolution HAADF-STEM images, we built geometrical atomic structure models for the free nanotwin and embedded nanotwin, illustrated in Fig. 1g,h, respectively. Figure 1g shows a free nanotwin formed on the Si wafer. As can be seen, all atoms maintain their normal arrangement except for an orientation difference. However, for embedded nanotwin, the GB is composed of some different structure units, such as a five-member ring and seven-member ring (equivalent on both sides of the embedded nanotwin), as illustrated in Fig. 1h. Herein, GB atoms are highlighted by different coloured balls for each layer. Experimentally, the atomic structure of the GB that we observed coincides with the model of the {112}  $\Sigma 3$  coincidence site lattice GB in Si<sup>34</sup>. The GB between main structure and embedded nanotwin is not a point defect but a plane defect, which exists around the entire embedded nanotwin (Supplementary Fig. 3).

### Theoretical evaluation of different twinning structures

To evaluate the effects of the above two types of defective structures on SHJ solar cells, the structures’ electronic properties were calculated via first-principles calculations<sup>35</sup>. Considering a large atomic number (756 Si atoms) in the supercell, we employed standard density functional theory (DFT) calculations to obtain the reasonable band structure, which is similar to the band structure calculated by hybrid DFT results (for a small system with around 50 atoms in the supercell). According to HAADF-STEM images and DFT optimization, we constructed polycrystalline Si structures with twin configurations and dislocation configurations, equivalent to free nanotwin and embedded nanotwin structures, respectively. Figure 2a–c shows three atomic models for single-crystalline Si, free nanotwin and embedded nanotwin structures. Figure 2d–f is the calculated band structures corresponding to Fig. 2a–c, respectively. As can be seen, the calculated band gap is ~0.63 eV for both single-crystalline Si (Fig. 2d) and the free nanotwin structure (Fig. 2e). This band gap value is consistent with previously reported results calculated by the same DFT method (all smaller than the experimental value of 1.17 eV)<sup>36,37</sup>, in which a generalized gradient approximation with the function of Perdew–Burke–Ernzerhof was adopted for a supercell. The similar calculated band gaps for single-crystalline Si and

the free nanotwin structure imply that there is no additional strain that can largely impact the band structure in bulk Si<sup>38</sup>. However, four additional gap states can be observed in the embedded nanotwin configuration (Fig. 2f). Two of them can be indexed as shallow defect states, which are close to the valence band maximum (marked by green curves). The other two are deep defect states in the middle between the valence band maximum and conduction band minimum (marked by red curves). Defects at deep states act as Shockley–Read–Hall non-radiative recombination centres, which may induce a short minority carrier lifetime<sup>39</sup>. On this basis, it can be concluded that the embedded nanotwin configuration should increase carrier recombination.

Furthermore, the densities of states for above three models are calculated, showing a good consistency with the results of calculated band structures (Supplementary Fig. 4). Figure 2g–i shows the partial charge densities associated with the states between the valence band maximum and conduction band minimum of the embedded nanotwin structure. Specifically, Fig. 2g,h shows the partial charge densities of two deep defect states and Fig. 2i shows that of a shallow defect state. We can find that charges are mainly localized around GB areas, which is the same as the locations of Si–Si bond disorder. As shown in Fig. 2j, Si–Si bond length at GBs ranges from the shortest value, 2.27 Å, to the longest value, 2.40 Å, while it stays at 2.37 Å (consistent with a previous report<sup>40</sup>) in other areas. This means that strain arises around the dislocation core at the GBs. Therefore, the defect states in Fig. 2g–i are consistent with the ones induced by strain. Such a case is similar to those reported in gallium arsenide, cadmium telluride and copper indium gallium selenide, where GBs generate deep levels in band gaps and are proved to be harmful to the performance of solar cells<sup>41,42</sup>. Therefore, our calculations suggest that free nanotwins at the c-Si/a-Si:H interface in a SHJ solar cell are benign, whereas embedded nanotwins are detrimental to the performance of the SHJ solar cells.

### The formation of embedded nanotwins

To reveal the origin and evolution of epitaxial growth in SHJ solar cells, c-Si/a-Si:H interface structures at different stages during cell fabrication are investigated by employing HRTEM. Figure 3a–d illustrates schematic diagrams representing four stages during cell fabrication, and Fig. 3e–h is the corresponding HRTEM images. Figure 3a is the stage after the native oxide on the Si wafer surface has been removed by hydrogen fluoride (HF) acid solution. Figure 3b,c represents the stages in which the i-a-Si:H layer and p-type a-Si:H (p-a-Si:H) layer have been deposited, respectively. Figure 3d shows the formation of front and rear silver electrodes. In Fig. 3e, a dashed yellow line is drawn to indicate a {111} plane of the c-Si wafer. As can be seen, the surface of c-Si is generally flat although some atomic steps are formed after cleaning by HF acid solution. However, an uneven interface appears in Fig. 3f and becomes rough in Fig. 3g–h, indicating that an epitaxial phenomenon occurs. Particularly, after the deposition of the i-a-Si:H layer shown in Fig. 3f, in addition to the atoms stacking that is compliant with the Si wafer (ABCABC..., the dashed white oval area), non-ABCABC... atom stacking also commences, as indicated by the dashed white rectangular areas. The latter is considered as a nucleation of the nanotwin. After the deposition of the p-a-Si:H layer, normal nucleation and nanotwin nucleation grow into some nano-islands, as shown in the dashed white areas of Fig. 3g. With the completion of silver (Ag) electrode preparation, different kinds of epitaxial islands gradually coalesce, resulting in the epitaxial layer being a continuous film with a mixed structure, in which some nanotwins (dashed white rectangular regions) are embedded, as shown in Fig. 3h.

### In situ observation of embedded nanotwin formation

To illustrate the evolutionary details of the c-Si/a-Si:H interface structure, we further performed *in situ* annealing experiments in TEM

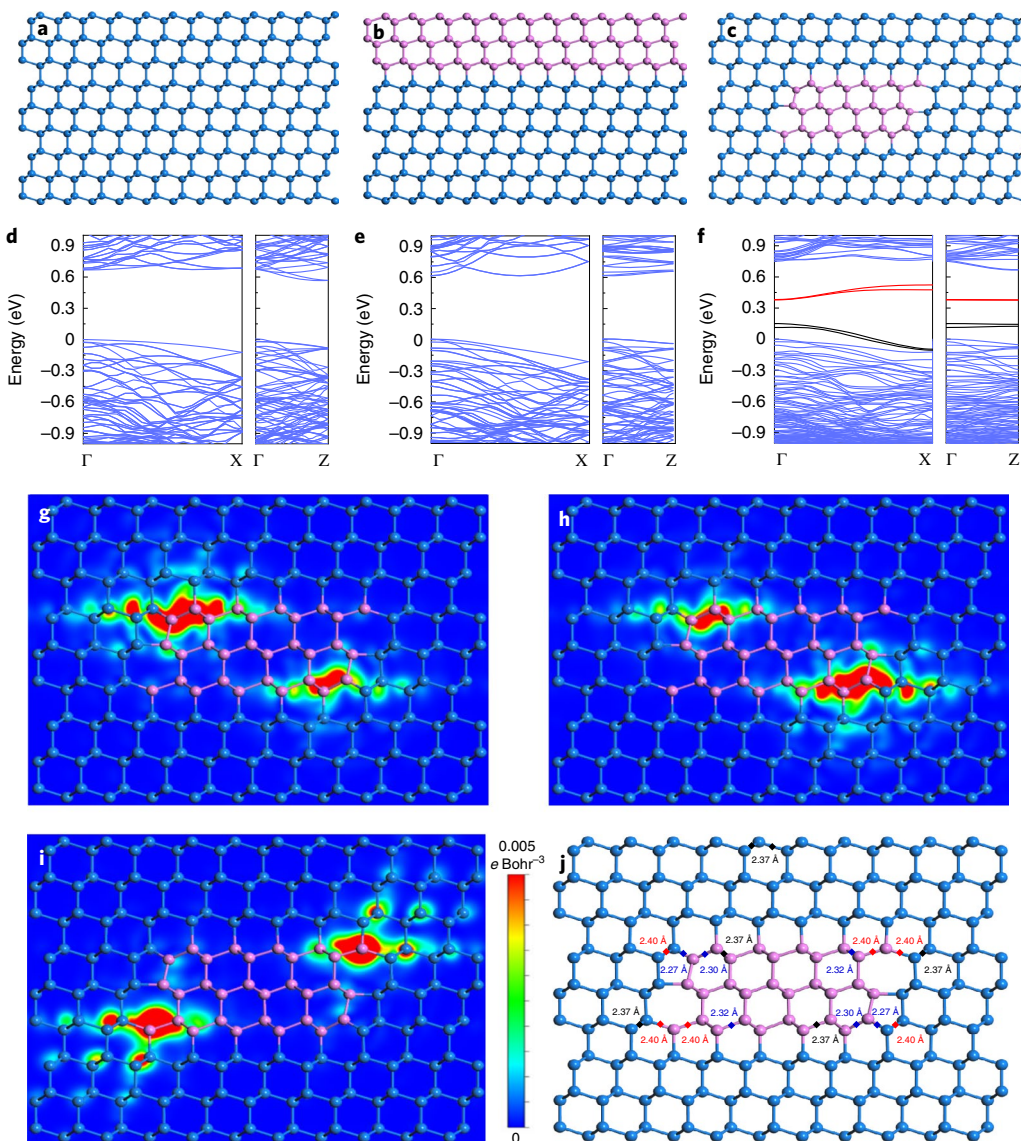


**Fig. 2 | Electronic structure characteristics of nanotwin configurations.** **a–c**, Equivalent atom models of single-crystalline silicon, free nanotwin and embedded nanotwin. The twin parts in the models are marked in pink comparing with the single-crystalline silicon wafer marked in blue. **d–f**, Calculated band structures corresponding to **a–c**, respectively. In **f**, shallow defect states and deep defect states are marked in black and red, respectively. **g–i**, Partial charge densities of deep defect states (**g–h**) and shallow defect states (**i**) in embedded nanotwin. Intensity colour plot from blue to red is scaled from low to high charge density. **j**, Strain distribution around GB areas in embedded nanotwin. The red, blue and black diamonds show tensile, compressive and normal bond lengths, respectively. For panels **g–j**, the embedded nanotwin is represented with pink balls, and the main structure is represented with blue balls.

by using a microelectromechanical systems (MEMS)-based heating system. A series of HRTEM images (Fig. 4) was recorded simultaneously when a lamella of a SHJ solar cell was being heated in a TEM instrument. In this *in situ* process, the heating profile includes steps at room temperature, 170 °C, 185 °C, 200 °C and 215 °C. Each step is prolonged for 30 minutes sequentially. In order to identify the same position during heating, a hole away from the interface was made by focusing the electron beam as the origin of the coordinate before heating (Supplementary Fig. 5). Therefore, the initial c-Si surface is uniquely determined during the heating process, as shown by the dashed white line in Fig. 4. From Fig. 4a–e, we can observe, with the temperature increasing, that the existing epitaxial layer continues to expand and some new epitaxial growth begin to appear. Specifically, Fig. 4f–o, which shows enlarged HRTEM images obtained from the areas marked by the dashed rose-red rectangle and the dashed aqua rectangle in Fig. 4a–e, respectively, further reveals the real-time

formation of embedded nanotwins. Figure 4f shows a nanotwin depicted by the dashed green lines, which is adjacent to the amorphous areas on its left and right sides, that is, the ‘free nanotwin’ mentioned earlier. With the temperature increasing, new epitaxial growth with the same stacking sequence as the c-Si wafer occurred on both sides of the free nanotwin, as highlighted with yellow dots. At the same time, the free nanotwin gradually expanded due to the epitaxial growth consistent with itself, which is highlighted with green dots. Eventually, an embedded nanotwin is formed when the two kinds of epitaxial layers with different stacking sequences meet each other, as shown in Fig. 4f–j. By contrast, in Fig. 4k, the epitaxial layer has the same structure as the c-Si wafer except for a disordered area surrounded by the dashed yellow curve. As the temperature increases, this disordered area evolves into different defect structures as shown in Fig. 4l–n. Finally, an embedded nanotwin is formed at 215 °C as depicted by the dashed green lines in Fig. 4o.

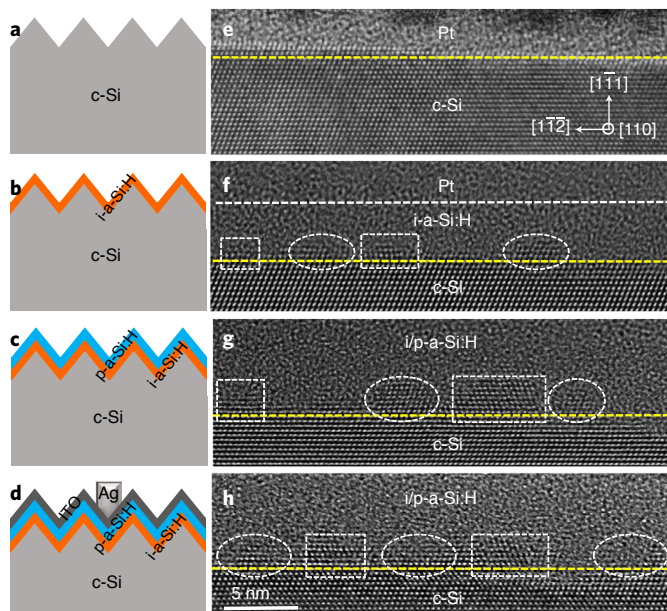


**Fig. 3 | c-Si/a-Si:H interface structures at different stages during cell preparation.** **a–d**, Schematic diagrams representing four stages during SHJ solar cells fabrication: after etching the surface of the Si wafer with HF acid solution (**a**); after the deposition of i-a-Si:H layer (**b**) and p-a-Si:H layer (**c**); and after the preparation of the Ag electrodes (**d**). **e–h**, HRTEM images of c-Si/a-Si:H interface corresponding to **a–d**. All HRTEM images were acquired along the  $\langle 110 \rangle$  direction. The dashed yellow lines indicate the  $\{111\}$  surface of the c-Si wafer. The dashed white line in **f** indicates the interface between the i-a-Si:H layer and Pt layer. The dashed rectangular/oval areas mark the atoms stacking twinned/compliant with the c-Si wafer. The i/p-a-Si:H indicates intrinsic and p-type amorphous Si deposited on c-Si surface in sequence. The scale bars are all 5 nm.

In this case, the embedded nanotwin evolves from the disordered region between two epitaxial layers with the same stacking sequence at a suitable annealing temperature. By comparison, another similar lamella taken from the same cell was heated at 175 °C for 2 hours. The result shows that there is not any formation of similar defect structures and only normal epitaxial growth (Supplementary Fig. 6). This indicates that the annealing temperature plays an important role in the formation of embedded nanotwins.

On the basis of ex situ and in situ HRTEM observations, the structural evolution of the Si wafer surface during the preparation of cells can be understood as follows. After RCA cleaning, a smooth  $\{111\}$  plane of Si wafer is formed. With the deposition of the i-a-Si:H layer, some crystal nuclei are formed due to the epitaxy of the amorphous Si at some sites of the interface. The nuclei are not identical because of the occurrence of different stacking sequences during the nucleation. Generally, epitaxial growth with an ideal stacking sequence will occur due to it having the lowest energy. However, the actual stacking sequence depends on many parameters, such as temperature, deposition rate, surface configuration and so on<sup>43</sup>. In the process, ideal nuclei are formed on the  $\{111\}$  plane by a correct ... ABCABCA stacking sequence. By contrast, a wrong atomic stacking may occur when the sequence is ...ABCACB, which leads to the appearance of a ‘twin seed’. Furthermore, based on the seed structure formed after the deposition of the i-a-Si:H layer, the epitaxial islands with normal structure or twinned structure can emerge under the effect of annealing during the deposition of a doped a-Si:H layer. At this stage, these epitaxial islands are usually surrounded by disordered atoms. Under further annealing treatment during the Ag electrode preparation process, the epitaxial islands continue to grow until the islands meet each other, leading to reconstructed boundaries. Specifically, if a normal island and a twinned island connect with each other, a  $\{112\} \Sigma 3$  twin boundary can form; that is, an embedded nanotwin can form. If two normal islands connect with each other, they are either integrated into a larger epitaxial island or separated by a disordered area that is similar to the morphology shown in Fig. 4k. However, it has been proved that the disordered

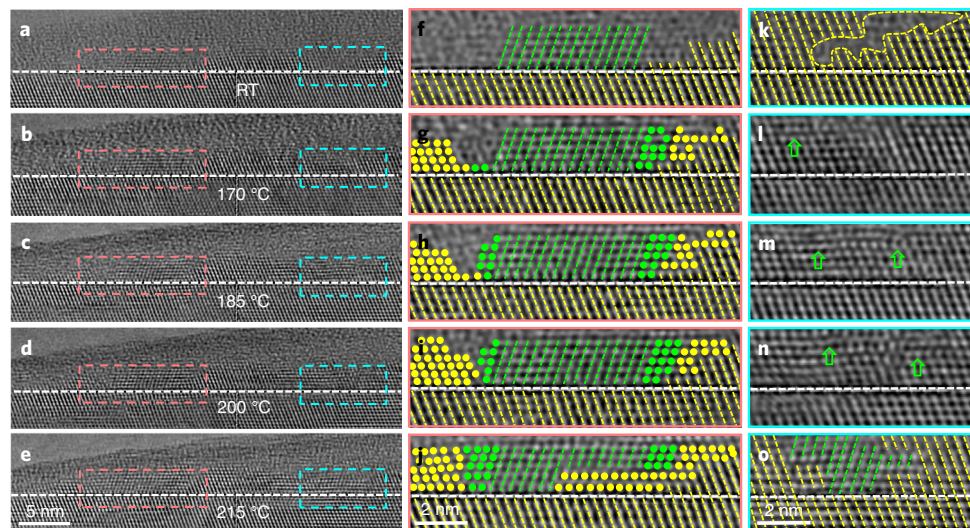


**Fig. 4 | HRTEM images showing structural evolution of c-Si/a-Si:H interface under heating.** A series of HRTEM images along the  $\langle 110 \rangle$  direction acquired after heating at different temperatures. Heating steps were carried out for 30 minutes. The dashed white lines indicate the initial c-Si surface. **a**, Initial c-Si/a-Si:H interface structure after the deposition of p-a-Si:H layer. RT, room temperature. **b–e**, c-Si/a-Si:H interface structure after heating at different temperatures. Scale bar in **e** applies to **a–e**. **f–o**, Magnified images corresponding to the dashed rose-red and aqua area rectangles in **a–e**. The dashed yellow and green lines depict the initial interface structure, representing the atoms stacking consistent and twinned with the silicon wafer, respectively. The yellow and green dots highlight the new epitaxial growth. The dashed curves in **k** indicate an amorphous area. Green hollow arrows in **l–n** mark some nanotwin nucleation during heating.

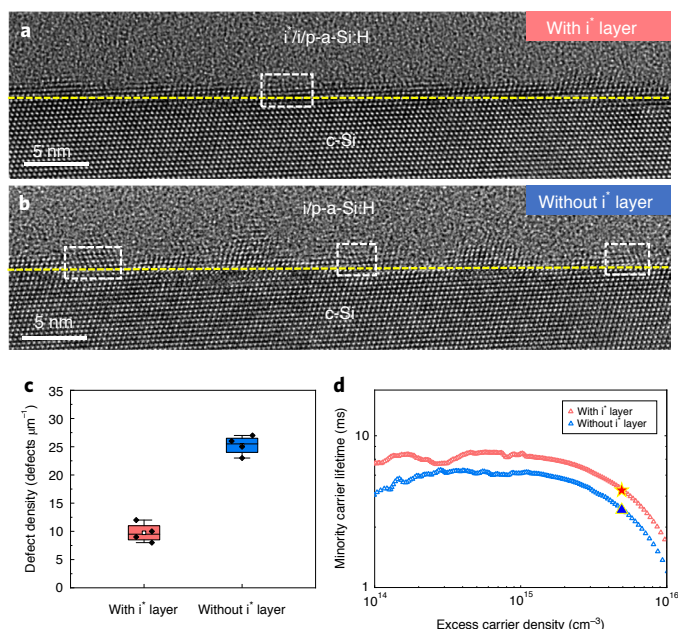


**Fig. 5 | The characteristics of two groups of SHJ solar cells with and without the i' layer.** **a,b**, Two HRTEM images showing the difference of the c-Si/a-Si:H interface structure in two groups of SHJ solar cells. The white dashed rectangles mark the position of the embedded nanotwins. **a**, The SHJ solar cell with i' layer. **b**, The SHJ solar cell without i' layer. The dashed yellow lines indicate the initial c-Si wafer surface and the dashed white rectangles mark the location of embedded nanotwins. i'/p-a-Si:H indicates three layers including i'-a-Si:H, standard i-a-Si:H and p-a-Si:H deposited on c-Si wafer in sequence. **c**, The linear density of embedded nanotwins at the c-Si/a-Si:H interface of two groups of SHJ solar cells, four cells per group. Rhombus symbols are the characteristic parameters of the SHJ solar cell. The distribution range of parameters are limited in the square, where the top, medium and bottom line represent maximum, median and minimum value, respectively. **d**, The  $\tau_{\text{eff}}$  of the passivated samples with and without the i' layer. The red star and solid blue triangle mark  $\tau_{\text{eff}}$  of the passivated samples with and without the i' layer at a carrier injection level of  $5 \times 10^{15} \text{ cm}^{-3}$ , respectively.

area is another source for the formation of embedded nanotwins at a suitable temperature.

### Reducing the density of embedded nanotwins

On the basis of the above analysis, we conclude that suppressing twin nucleation in the initial stages is the critical step in reducing embedded nanotwins. To achieve that, before standard i-a-Si:H layer deposition, an ultra-thin (less than 1 nm) i-a-Si:H buffer layer (marked as the i' layer) was grown by radio-frequency plasma-enhanced chemical vapour deposition using pure SiH<sub>4</sub> at a deposition rate of about 2 Å s<sup>-1</sup>. For comparison, standard i-a-Si:H layers, with the same total thickness, were grown on a different group of cells. Except for this i' layer configuration, these two groups of cells have identical process conditions, including the standard i-a-Si:H, doped amorphous/microcrystal Si/SiO<sub>x</sub>:H and indium tin oxide layers, as well as Ag grid electrodes. These fabrication conditions were identical to that of the 24.85% cell. In order to focus on the impact of the c-Si/a-Si:H interface on the performances of cells, several fabrication steps, such as the antireflection coating, were avoided for both groups. After introducing the i' layer, an average 2.5 mV enhancement in  $V_{\text{OC}}$  and average 0.32% enhancement in FF are obtained, as well as a slight increase of short circuit current ( $I_{\text{SC}}$ ). Eventually, an average ~0.32% absolute improvement of PCE is achieved (Supplementary Fig. 7).

The c-Si/a-Si:H interface structures of the two groups, with and without the i' layer, are investigated in Fig. 5a,b, respectively. Both the number and volume of embedded nanotwins at the c-Si/a-Si:H interface of the cell with the i' layer are greatly reduced. The statistics of more samples are shown in Supplementary Fig. 8. Moreover, the linear density of nanotwins is reduced from ~25 to ~10 per micrometre (Fig. 5c). Figure 5d shows the minority carrier lifetime ( $\tau_{\text{eff}}$ ) of two passivated samples prepared with and without the ultra-thin i' layer. At a carrier injection level of  $5 \times 10^{15} \text{ cm}^{-3}$ ,  $\tau_{\text{eff}}$  increases from 3.2 ms to 4.3 ms after introducing the i' layer. The implied  $V_{\text{OC}}$  ( $iV_{\text{OC}}$ ) increases from 746.5 mV (without the i' layer) to 751.9 mV (with the i' layer). These results confirm an important correlation between the density of embedded nanotwins at the c-Si/a-Si:H interface and the interface recombination. Specifically, reducing embedded nanotwins at the c-Si/a-Si:H interface can obviously reduce the carrier recombination at the interface. Other interface recombination parameters, such as the saturation current density ( $J_{\text{os}}$ ), show good consistency with the improvement of  $\tau_{\text{eff}}$ . Relevant calculations are described in the Methods.

By comparing the SHJ/interdigitated-back-contact cell efficiency,  $\eta = 26.3\%$  with the theoretical highest PCE,  $\eta^{\text{theo}} = 29.1\%$ , an excellent loss analysis was performed to point out a path towards the theoretical limit<sup>5</sup>. Following this method, we investigated PCE losses between  $\eta^{\text{theo}} = 29.1\%$  and the highest performing cell from each group:  $\eta^1 = 24.58\%$  (with i' layer) and  $\eta^2 = 24.10\%$  (without i' layer). After the introduction of the i' layer, the extrinsic recombination loss is reduced by ~33% (absolute PCE loss changes from 1.2% to 0.8%) compared to the cell without the i' layer (Methods). This value is in good agreement with the  $\tau_{\text{eff}}$  improvement of 34.4%. Since the introduction of the i' layer induces an obvious reduction of nanotwins at the c-Si/a-Si:H interface, it can be concluded that the reduction of nanotwins is crucial for improving the PCE of SHJ solar cells.

### Exploring to further reduce the density of nanotwins

By adjusting the deposition process of the i-a-Si:H layer, a c-Si/a-Si:H interface with low-density embedded nanotwins has been obtained, which improves the cell performance significantly. Therefore, we further explore how to eliminate this defective structure as much as possible. In our experiments, we also find that the nanotwins are more apt to form on a c-Si surface that is exactly a {111} plane during the fabrication of SHJ solar cells. However, when the c-Si surface deviates from a {111} plane, the nucleation of nanotwins at the c-Si surface could become difficult. Figure 6a,b exhibits the interface structures with different Si wafer surfaces after depositing the i-a-Si:H layer. In Fig. 6a, the c-Si surface is parallel to the {111} plane and two twin seeds form on it. However, there is hardly any twin nucleation on the c-Si surface shown in Fig. 6b, which is slightly askew from the {111} plane. Furthermore, this tendency can also be verified by the interface structure in a full SHJ solar cell (Supplementary Fig. 9).

In fact, such a phenomenon could be attributed to the fact that the surface deviated from the {111} plane is composed of numerous {111} facets and other facets, which means that the surface is no longer atomically flat but has a series of atomic steps. When the epitaxy occurs, the atomic arrangement at the corners of atomic steps adopts the normal stacking sequences instead of the form of twin seeds in order to reduce energy. Under further annealing processes, the epitaxial growth can proceed with the stacking sequence unchanged. However, if the surface is an exact {111} plane, wrong stacking sequences can happen easily, leading to the formation of nanotwins on the c-Si surface. A schematic diagram for such a process is summarized in Fig. 6c. Our experimental observations agree well with the results from a molecular dynamics simulation for twin formation on different Si planes<sup>44</sup>. Therefore, embedded nanotwins at the c-Si/a-Si:H interface can be further reduced by modifying the

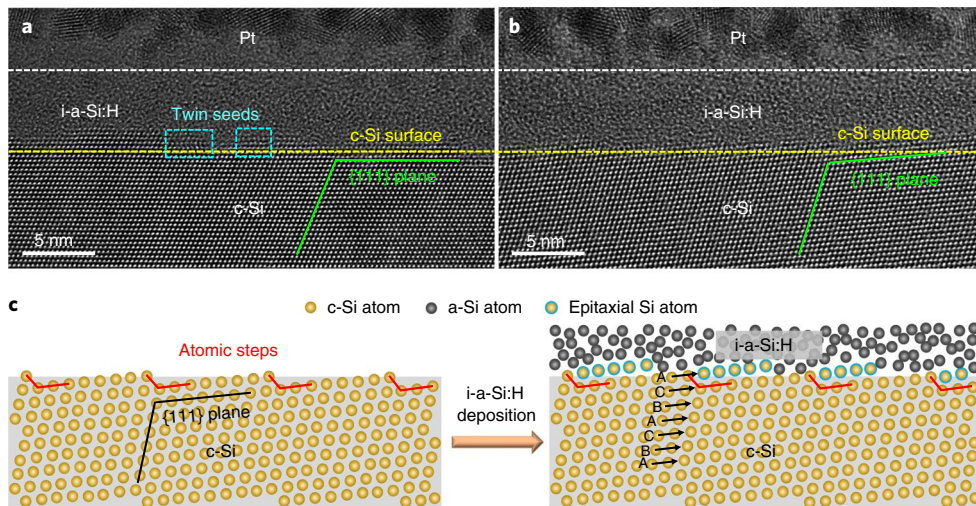


**Fig. 6 | The effect of surface configuration of Si wafer on formation of nanotwin.** **a,b**, Two HRTEM images showing different interface structure after depositing i-a-Si:H layer. **a**, c-Si surface is parallel to {111} plane. **b**, c-Si surface deviates from {111} plane. The dashed yellow lines indicate the initial c-Si wafer surface and the dashed blue rectangles in **a** mark the location of nanotwin nucleation. The dashed white lines indicate the interface between the i-a-Si:H layer and Pt layer. **c**, Schematic diagram showing the structural evolution of the c-Si surface, deviated from the {111} plane when depositing the i-a-Si:H layer. The grey shading in **c** shows a schematic shape of the Si wafer, and the balls represent Si atoms. Four atomic steps are presented on the c-Si surface by the red angled lines. ABCABC denotes the stacking sequences during epitaxy nucleation.

initial surface configuration of the c-Si wafer. Undoubtedly, in this surface engineering, further precise control of texturing and cleaning processes would be necessary.

## Conclusion

The c-Si/a-Si:H interface structure of high-efficiency SHJ cells fabricated by industrially compatible processes are investigated via  $C_s$ -corrected TEM. Atomic-resolution HAADF-STEM images clearly show that high-density embedded nanotwins commonly exist in the epitaxial layer, which produces extra deep defect levels and impairs the performance of SHJ solar cells. Ex situ and in situ HRTEM experiments uncover that the nanotwin seeds are generated during the deposition of the i-a-Si:H layer, and the growth proceeds with high annealing temperature. To suppress the formation of such embedded nanotwins, an ultra-thin i' buffer layer is introduced prior to the deposition of the normal i-a-Si:H layer, resulting in an improvement of  $\tau_{\text{eff}}$ . At the atomic level, this work draws attention to the growth of detrimental nanotwins in the epitaxial layer for the Si semiconductor industry. It provides an approach to mitigate the defects to further improve the performance of SHJ solar cells.

## Methods

**SHJ solar cell fabrication.** SHJ solar cells were fabricated by adopting Hanergy's preparation process, which created a record 24.85% PCE with a  $244.5 \text{ cm}^2$  total area in 2019. A commercial M2 Czochralski-grown n-type <100> oriented Si wafer was used as the starting substrate, which has a thickness of  $150 \mu\text{m}$  and a resistivity of  $\sim 3\text{--}5 \Omega\text{cm}$ . First, in order to increase the light trapping effect, pyramid structures were formed by chemically texturing the two surfaces of the Si wafer. This was followed by the RCA cleaning process of the wafer. Second, the native oxide on the wafer surfaces was removed using HF acid solution. Third, using a very-high-frequency plasma-enhanced chemical vapour deposition technique at 40.68 MHz, intrinsic amorphous Si:H (i-a-Si:H) passivation layers were deposited on both sides of the c-Si wafer, and then an n-type microcrystalline  $\text{SiO}_x\text{H}$  (n- $\mu\text{-SiO}_x\text{H}$ ) layer and p-type amorphous Si:H (p-a-Si:H) layer were deposited on the front and rear sides, respectively. Fourth, the indium tin oxide layers were sputtered on both sides of the cells to enhance the carrier lateral transportation and collection by a magnetron sputtering method. Finally, annealing at  $190^\circ\text{C}$  for 30 min was employed to form the front and the rear silver electrodes on the indium tin oxide surfaces by a screen printing method.

**TEM sample preparation.** TEM samples were prepared by cutting the pyramid structures on the rear surface of the SHJ solar cell in an FEI Helios-600i Nanolab

FIB/scanning-electron-microscopy (FIB/SEM) system. The sampling position is shown in the dashed yellow rectangular area in Supplementary Fig. 10a. Before cutting cross-sectional samples from the SHJ solar cell devices in the FIB chamber, a platinum layer was deposited on the surface of the pyramid structure using an electron beam and ion beam sequentially in order to avoid damage to the cross-sectional samples by the ion beam during sample preparation. The reason for first using an electron beam to induce the deposition is that electron-beam-induced deposition offers the advantage of not sputtering the deposited material or implanting gallium simultaneously. To obtain high-quality HRTEM/STEM images, the thickness of the lamellae is thinned to  $\sim 20\text{--}30 \text{ nm}$  in the end. Supplementary Fig. 10b is a SEM image showing the cross-sectional structure of the SHJ solar cell. Supplementary Fig. 10c is a TEM image showing the interface structure of the SHJ solar cell.

In particular, the samples for in situ heating in TEM were obtained from the stage after the deposition of the p-a-Si:H layer. In the process, a lamella was first prepared according to the method mentioned above, and then it was transferred onto a MEMS chip (commercially available wildfire  $\text{SiN}_x$  nano-chip, DENNsolutions) in the FIB system. Supplementary Fig. 11a,b shows the schematic diagram of the MEMS-based heating system. Supplementary Fig. 11c is a SEM image showing that a sample lamella is fixed in the nano-chip eventually. With the help of the MEMS-based heating system, we can observe the structural evolution of the c-Si/a-Si:H interface at the atomic level simultaneously during the heating process in the TEM instrument.

**Ex situ and in situ TEM characterization.** HRTEM and HAADF-STEM images were acquired by employing an FEI Titan ETEM with an image  $C_s$ -corrector and an FEI Titan Themis TEM instrument with a probe  $C_s$ -corrector, respectively, both operating at  $300 \text{ kV}$  acceleration voltage. In situ heating experiments in TEM were performed using the DENNsolutions TEM holder system, in which temperature accuracy, temperature stability and temperature homogeneity are better than 95%,  $0.005^\circ\text{C}$  and 99.5%, respectively.

**Theoretical calculation.** Calculations of the electronic properties were performed with first-principles DFT, as implemented in the Vienna Ab initio Simulation Package<sup>45</sup>. The generalized gradient approximation with the function of Perdew-Burke-Ernzerhof was employed to describe the exchange-correlation interactions<sup>46</sup>. A cut-off of plane-wave kinetic energy of  $400 \text{ eV}$  was taken, and the convergence of total energy via the self-consistent field method was set to  $10^{-4} \text{ eV}$ . All atomic position and lattice parameters were optimized, and the atomic forces were less than  $0.01 \text{ eV } \text{\AA}^{-1}$ . Three equilibrium structures with a  $14 \times 9 \times 6$  supercell, including (1) single-crystalline Si, (2) polycrystalline Si with a twin configuration and (3) polycrystalline Si with a dislocation configuration, were constructed, and their band structure and density of states were investigated by using ab initio calculations. The partial charge densities of defect states for the embedded nanotwin were visualized via the visualization for electronic and structures analysis (VESTA) software package<sup>47</sup>.

**Saturation current density calculation.** Recombination parameters, such as the dark saturation current density ( $J_{0s}$ ), can be extracted from  $\tau_{\text{eff}}$  measurement. In equation (1),  $q$  is the elementary charge,  $n_i$  is the intrinsic carrier density and  $W$  represents the substrate thickness<sup>48</sup>.  $\tau_{\text{bulk}}$  is the carrier lifetime from Si substrate.  $N_D$  is the doping density of the substrate ( $1.5 \times 10^{15} \text{ cm}^{-3}$ ).  $J_{0sf}$  and  $J_{0sb}$  represent the front and back  $J_{0s}$  and are assumed to be identical in the symmetrical structure used in this study.

$$\frac{1}{\tau_{\text{eff}}} = \frac{1}{\tau_{\text{bulk}}} + \frac{J_{0sf} + J_{0sb}}{qn_i^2 W} (N_D + \Delta n) \quad (1)$$

A lifetime tester WCT-120 (Sinton Instruments, with transient mode at 25 °C) was used for  $\tau_{\text{eff}}$  measurements. We first plot the inverse Auger-corrected lifetime as a function of excess carrier concentration ( $\Delta n$ ) in Supplementary Fig. 12 (Auger model of Sinton). The  $J_{0s}$  was then extracted from the slope ( $K$ ) of curves in Supplementary Fig. 12 in the injection range  $3 \times 10^{15} \text{ cm}^{-3} < \Delta n < 6 \times 10^{15} \text{ cm}^{-3}$  following the method of Kane and Swanson<sup>49,50</sup>:

$$J_{0s} = \frac{qn_i^2 W}{2} K \quad (2)$$

We estimate a  $J_{0s}$  of  $1.9 \text{ fA cm}^{-2}$  and  $3.7 \text{ fA cm}^{-2}$  for the passivated samples with and without the i' layer.

**PCE loss analysis.** Following the method adopted in ref.<sup>5</sup>, we analysed the absolute conversion efficiency difference between  $\eta^{\text{theo}} = 29.1\%$  (theoretical efficiency limit of a Si solar cell with a thickness of  $165 \mu\text{m}$  and resistivity of  $3 \Omega \text{ cm}$ ) and the actual efficiency obtained by SHJ solar cells ( $\eta^{\text{w/o i' layer}} = 24.1\%$  for a SHJ solar cell without the i' layer,  $\eta^{\text{w/i' layer}} = 24.58\%$  for a SHJ solar cell with the i' layer), as shown in Supplementary Table 1.

Compared with the theoretical limit of  $V_{OC}^{\text{theo}} = 0.752 \text{ V}$ , there is room to improve 1.2% (9 mV) and 0.8% (6.2 mV) for the  $V_{OC}$  of the SHJ solar cell without and with i' layer, respectively. These differences result from the surface recombination and Shockley–Read–Hall recombination.

The  $J_{SC}$  values obtained from the SHJ solar cell without and with the i' layer are  $39.0 \text{ mA cm}^{-2}$  and  $39.3 \text{ mA cm}^{-2}$ , which are 10.9% and 10.1% lower, respectively, than the theoretical limit  $J_{SC}^{\text{theo}}$  of  $43.7 \text{ mA cm}^{-2}$ . The lower  $J_{SC}$  can be attributed to the grid shadow, surface reflection and parasitic absorption.

The FF values of 83.3% (without the i' layer) and 83.9% (with the i' layer) are 5.9% and 5.2% lower, respectively, than the theoretical value of 88.5%. Suns– $V_{OC}$  measurements were utilized to analyse the FF loss caused by series resistance ( $R_s$ )<sup>51</sup>. Pseudo FF (pFF; FF without  $R_s$  influence) values of 85.9% (without the i' layer) and 86.4% (with the i' layer) were obtained. The resistive loss relative to the theoretical limit is estimated to be 2.9% and 2.8% using  $(\text{pFF} - \text{FF}_{\text{actual}})/\text{FF}_{\text{theo}}$ , where FF<sub>actual</sub> and FF<sub>theo</sub> are the actual and theoretical FF values, respectively. The remaining 3.0% and 2.4% loss for FF can originate from recombination, such as SRH and surface recombination for nonideal interface passivation or shallow level defects. Eventually, absolute efficiency losses with respect to the theoretical limit are compared with SHJ solar cells without and with the i' layer, as shown in Supplementary Fig. 13. Extrinsic recombination loss is improved by ~0.4% after introducing the i' layer to reduce nanotwins.

## Data availability

All data generated or analysed during this study are included in the published article and its Supplementary Information. Source data are provided with this paper.

Received: 7 May 2020; Accepted: 16 December 2020;

Published online: 8 February 2021

## References

- Battaglia, C., Cuevas, A. & de Wolf, S. High-efficiency crystalline silicon solar cells: status and perspectives. *Energy Environ. Sci.* **9**, 1552–1576 (2016).
- Haschke, J., Dupré, O., Boccard, M. & Ballif, C. Silicon heterojunction solar cells: recent technological development and practical aspects – from lab to industry. *Sol. Energy Mater. Sol. Cells* **187**, 140–153 (2018).
- Trube, J. *International Technology Roadmap for Photovoltaic (ITRPV): Eleventh Edition Online* (2020); <https://itrv.vdma.org/viewer/-/v2/article/render/48393879>
- Richter, A., Hermle, M. & Glunz, S. W. Reassessment of the limiting efficiency for crystalline silicon solar cells. *IEEE J. Photovolt.* **3**, 1184–1191 (2013).
- Yoshikawa, K. et al. Silicon heterojunction solar cell with interdigitated back contacts for a photoconversion efficiency over 26%. *Nat. Energy* **2**, 17032 (2017).
- Fuhs, W., Niemann, K. & Stuke, J. Heterojunctions of amorphous silicon and silicon single crystals. *AIP Conf. Proc.* **20**, 345–350 (1974).
- De Wolf, S., Descoeudres, A., Holman, Z. C. & Ballif, C. High-efficiency silicon heterojunction solar cells: a review. *Green* **2**, 7–24 (2012).
- Adachi, D., Hernández, J. L. & Yamamoto, K. Impact of carrier recombination on fill factor for large area heterojunction crystalline silicon solar cell with 25.1% efficiency. *Appl. Phys. Lett.* **107**, 233506 (2015).
- Green, M. A. et al. Solar cell efficiency tables (version 51). *Prog. Photovoltaics Res. Appl.* **26**, 3–12 (2018).
- Yamamoto, K., Yoshikawa, K., Uzu, H. & Adachi, D. High-efficiency heterojunction crystalline Si solar cells. *Jpn. J. Appl. Phys.* **57**, 08RB20 (2018).
- Essig, S. et al. Raising the one-sun conversion efficiency of III–V/Si solar cells to 32.8% for two junctions and 35.9% for three junctions. *Nat. Energy* **2**, 17144 (2017).
- Bush, K. A. et al. 23.6%-efficient monolithic perovskite/silicon tandem solar cells with improved stability. *Nat. Energy* **2**, 17009 (2017).
- Hekmatshoar, B., Shahrijerdi, D., Hopstaken, M., Ott, J. A. & Sadana, D. K. Characterization of thin epitaxial emitters for high-efficiency silicon heterojunction solar cells. *Appl. Phys. Lett.* **101**, 103906 (2012).
- de Wolf, S., Ballif, C. & Kondo, M. Kinetics of a-Si:H bulk defect and a-Si:H/c-Si interface-state reduction. *Phys. Rev. B* **85**, 113302–113306 (2012).
- Park, J. S., Kim, S., Xie, Z. & Walsh, A. Point defect engineering in thin-film solar cells. *Nat. Rev. Mater.* **3**, 194–210 (2018).
- Li, H. et al. The amorphous/crystalline silicon interface research of HIT solar cells by simulation. *Adv. Mater. Res.* **773**, 124–131 (2013).
- Pankove, J. I. & Tarnig, M. L. Amorphous silicon as a passivant for crystalline silicon. *Appl. Phys. Lett.* **34**, 156 (1979).
- Fujiwara, H. & Kondo, M. Impact of epitaxial growth at the heterointerface of a-Si:H/c-Si solar cells. *Appl. Phys. Lett.* **90**, 013503 (2007).
- Descoeudres, A. et al. Improved amorphous/crystalline silicon interface passivation by hydrogen plasma treatment. *Appl. Phys. Lett.* **99**, 123506 (2011).
- Yan, Y. et al. Atomic structure and electronic properties of c-Si/a-Si:H heterointerfaces. *Appl. Phys. Lett.* **88**, 121925 (2006).
- Geissbühler, J. et al. Amorphous/crystalline silicon interface defects induced by hydrogen plasma treatments. *Appl. Phys. Lett.* **102**, 231604 (2013).
- Ali, H. et al. Thermal stability of hole-selective tungsten oxide: in situ transmission electron microscopy study. *Sci. Rep.* **8**, 12651 (2018).
- Ali, H. et al. In situ transmission electron microscopy study of molybdenum oxide contacts for silicon solar cells. *Phys. Stat. Sol. A* **216**, 1800998 (2019).
- Fan, Z. et al. In situ transmission electron microscopy for energy materials and devices. *Adv. Mater.* **31**, 1900608 (2019).
- Urban, K. W. Studying atomic structures by aberration-corrected transmission electron microscopy. *Science* **321**, 506–510 (2008).
- Sun, J. et al. Liquid-like pseudoelasticity of sub-10-nm crystalline silver particles. *Nat. Mater.* **13**, 1007–1012 (2014).
- Divitini, G. et al. In situ observation of heat-induced degradation of perovskite solar cells. *Nat. Energy* **1**, 15012 (2016).
- Zou, L., Li, J., Zakharov, D., Stach, E. A. & Zhou, G. In situ atomic-scale imaging of the metal/oxide interfacial transformation. *Nat. Commun.* **8**, 307 (2017).
- Gong, Y. et al. Three-dimensional atomic-scale observation of structural evolution of cathode material in a working all-solid-state battery. *Nat. Commun.* **9**, 3341 (2018).
- Zhao, H. et al. Atomic-scale understanding of stress-induced phase transformation in cold-rolled Hf. *Acta Mater.* **131**, 271–279 (2017).
- Hao, M. et al. Ligand-assisted cation-exchange engineering for high-efficiency colloidal  $\text{Cs}_1\text{FA}_x\text{PbI}_3$  quantum dot solar cells with reduced phase segregation. *Nat. Energy* **5**, 79–88 (2020).
- Wang, T. H. et al. Effect of emitter deposition temperature on surface passivation in hot-wire chemical vapor deposited silicon heterojunction solar cells. *Thin Solid Films* **501**, 284–287 (2006).
- Zhu, Y. et al. Unravelling surface and interfacial structures of a metal-organic framework by transmission electron microscopy. *Nat. Mater.* **16**, 532–536 (2017).
- Sakaguchi, N., Ichinose, H. & Watanabe, S. Atomic structure of faceted  $\Sigma 3$  CSL grain boundary in silicon HRTEM and *ab-initio* calculation. *Mater. Trans.* **48**, 2585–2589 (2007).
- Neaton, J. B., Muller, D. A. & Ashcroft, N. W. Electronic properties of the Si/SiO<sub>2</sub> interface from first principles. *Phys. Rev. Lett.* **85**, 1298–1301 (2000).
- Ramos, L. E. et al. Structural, electronic, and effective-mass properties of silicon and zinc-blende group-III nitride semiconductor compounds. *Phys. Rev. B* **63**, 165210 (2001).
- Deák, P., Aradi, B., Frauenheim, T., Janzén, E. & Gali, A. Accurate defect levels obtained from the HSE06 range-separated hybrid functional. *Phys. Rev. B* **81**, 153203 (2010).
- Huebl, H. et al. Phosphorus donors in highly strained silicon. *Phys. Rev. Lett.* **97**, 166402 (2006).
- Yin, W. J., Shi, T. & Yan, Y. Unique properties of halide perovskites as possible origins of the superior solar cell performance. *Adv. Mater.* **26**, 4653–4658 (2014).
- Vogt, P. et al. Silicene: compelling experimental evidence for graphenelike two-dimensional silicon. *Phys. Rev. Lett.* **108**, 155501 (2012).

41. Zhang, L. et al. Effect of copassivation of Cl and Cu on CdTe grain boundaries. *Phys. Rev. Lett.* **101**, 155501 (2008).
42. Abou-Ras, D. et al. Confined and chemically flexible grain boundaries in polycrystalline compound semiconductors. *Adv. Energy Mater.* **2**, 992–998 (2012).
43. Meinel, K., Klaua, M. & Bethge, H. On twin and stacking fault formation during the epitaxial film growth of F.C.C. materials on (111) substrates. *Phys. Stat. Sol.* **110**, 189–196 (1988).
44. Zhai, S. et al. The twin formations on different growth planes of silicon crystal growth from melt by a molecular dynamics study. *Phys. B* **572**, 184–189 (2019).
45. Kresse, G. & Hafner, J. *Ab initio* molecular dynamics for liquid metals. *Phys. Rev. B* **47**, 558–561 (1993).
46. Perdew, J. P., Burke, K. & Ernzerhof, M. Generalized gradient approximation made simple. *Phys. Rev. Lett.* **77**, 3865–3868 (1996).
47. Momma, K. & Izumi, F. VESTA: a three-dimensional visualization system for electronic and structural analysis. *J. Appl. Crystallogr.* **41**, 653–658 (2008).
48. Kimmerle, A., Rothhardt, P., Wolf, A. & Sinton, R. A. Increased reliability for  $J_0$ -analysis by QSSPC. *Energy Procedia* **55**, 101–106 (2014).
49. Mäckel, H. & Varner, K. On the determination of the emitter saturation current density from lifetime measurements of silicon devices. *Prog. Photovoltaics Res. Appl.* **21**, 850–866 (2012).
50. Janssen, G. J. M., Wu, Y., Tool, K. C. J. J., Romijn, I. G. & Fell, A. Extraction of recombination properties from lifetime data. *Energy Procedia* **92**, 88–95 (2016).
51. Augusto, A., Herasimenka, S. Y., King, R. R., Bowden, S. G. & Honsberg, C. Analysis of the recombination mechanisms of a silicon solar cell with low bandgap-voltage offset. *J. Appl. Phys.* **121**, 205704 (2017).

## Acknowledgements

This work was financially supported by the National Natural Science Foundation of China (no. 11774016, 61922005, 11874314 and 62034001), Beijing Great Wall

Scholars Program, Beijing Academic Outstanding Young Scientists Projects (BJWZYJH01201910005018) and Australian Research Council. We thank Y. Zhang, M. Yang and C. Yu for device fabrication and SHJ cell process development, X. Chen for theoretical calculations and Y. Qin for SEM characterization from Carl Zeiss.

## Author contributions

X.Q. prepared the TEM sample and executed aberration-corrected HRTEM and HAADF-STEM. Y.H., M.Q. and T.R. fabricated the devices and carried out photovoltaic characterization. F.C. and Z.Z. carried out theoretical calculations. Y.M and Y.C. assisted with the theoretical calculations. X.R. assisted in the fabrication of devices. X.Q., Y.Z. and K.Z. analysed the experimental results and wrote the manuscript. X.X., H.Y. and Lihua Wang made helpful comments on the manuscript. X.H., Z.H., Z.-G.C. and Lianzhou Wang guided the PCE loss analysis and provided constructive suggestions. K.Z. and Y.Z. led the entire project. All authors read the manuscript and contributed to the discussion of the results.

## Competing interests

The authors declare no competing interests.

## Additional information

**Supplementary information** is available for this paper at <https://doi.org/10.1038/s41560-020-00768-4>.

**Correspondence and requests for materials** should be addressed to Y.Z. or K.Z.

**Peer review information** *Nature Energy* thanks Urs Aeberhard, Kristopher Davis and the other, anonymous, reviewer(s) for their contribution to the peer review of this work.

**Reprints and permissions information** is available at [www.nature.com/reprints](http://www.nature.com/reprints).

**Publisher's note** Springer Nature remains neutral with regard to jurisdictional claims in published maps and institutional affiliations.

© The Author(s), under exclusive licence to Springer Nature Limited 2021